A sheared low-rank model for oblique stripe removal

Jian-Li Wang [a], Ting-Zhu Huang [a,*], Tian-Hui Ma [b], Xi-Le Zhao [a,*], Yong Chen [a]

[a] School of Mathematical Sciences/Research Center for Image and Vision Computing, University of Electronic Science and Technology of China, Chengdu, Sichuan 611731, PR China
[b] School of Mathematics and Statistics/Research Center for Image and Vision Computing, Xi'an Jiaotong University, Xi'an, Shaanxi 710049, PR China

A B S T R A C T

Stripe noise removal from remote sensing imagery is a key preprocessing step for many applications, such as urban planning, military, and environmental monitoring. Two significant priors of the stripe are low-rankness and group sparsity, which play a central role in many destriping methods. However, for oblique stripes, these two priors are no longer explicitly applicable. To overcome this difficulty, we propose a novel sheared decomposition framework for oblique stripe removal. The main idea is to perform a shear operation on the observed image, so that the oblique stripe is transformed to nearly vertical lines. For the stripe component, we characterize the low-rankness and group sparsity priors in the sheared domain. For the image component, we characterize the smoothness prior in the original domain by unidirectional total variation (UTV), which can preserve the strong edges and geometric features while suppressing stripes. To solve the proposed model, we design an efficient alternating direction method of multipliers (ADMM) algorithm with guaranteed convergence. Experiments using simulated and real data show that the proposed method can remove the oblique stripe effectively and outperform the state-of-the-art methods qualitatively and quantitatively.

© 2019 Elsevier Inc. All rights reserved.

1. Introduction

Remote sensing imagery has been widely used in urban planning, military, environmental monitoring, and many other fields. However, during the imaging process, the observed image is inevitably contaminated by the stripe noise, due to dropping lines during scanning, differences between forward and reverse scanning, and variations in calibrations across sensor arrays in multisensor instruments [18,24]. The stripe noise not only greatly degrades the image quality, but also results in low accuracy in segmentation [22] and target detection [40]. Therefore, destriping is a key preprocessing before the applications of remote sensing imagery.

For the vertical (horizontal) stripe, existing destriping methods can be roughly divided into four categories: digit filtering-based methods, statistics-based methods, optimization-based methods, and learning-based method. Filtering-based methods suppressed the stripe noise by constructing a filter on a transformed domain, such as Fourier transform [14,35], wavelet analysis [43], and the combined domain filter [33,36]. Statistics-based methods mainly relied on the statistical properties of digital number for each sensor [6,21,24,37,41,48], such as moment matching [21,41] and histogram matching [24,48].

---

* Corresponding authors.
E-mail addresses: wangjianli_123@163.com (J.-L. Wang), tingzhuhuang@126.com (T.-Z. Huang), nkmth0307@126.com (T.-H. Ma), xlzhao122003@163.com (X.-L. Zhao), chenyong1872008@163.com (Y. Chen).

Optimization-based methods regarded destriping as an ill-posed inverse problem and performed destriping by solving regularization models [1,3,7–9,11,16,17,29,30,38,44,45,52,54,56,57], such as anisotropic spectral-spatial total variation (TV) model [9], the improved unidirectional total variation (UTV) models [7,8,25,27,45,50,52,56], low-rank models [11,26,28,30,31,55], and global sparsity models [15,16,29,42,46]. Recently, learning-based method [10] introduced the deep convolutional neural network (CNN) for destriping to extract the spatial information of stripe in an adaptive way. Although the above methods perform well in dealing with the vertical stripe, they are no longer explicitly applicable for oblique stripe removal. This is mainly because the oblique stripe does not exhibit most priors for the vertical stripe, such as group sparsity and low-rankness.

For the oblique stripe, existing destriping methods can be mainly divided into three classes: filtering-based methods [13,18,23,39], histogram matching-based methods [21,24,48,49], and the transformed low-rankness-based method [12]. Filtering-based methods constructed filters to remove most frequency components produced by the oblique stripe at a given frequency. But they also removed some frequency components caused by the non-stripe image information at the same time, resulting in the poor representation ability for the periodic stripe. Histogram-based methods dealt with the stripe noise by matching the histogram of each subscene to the histogram of the overall image, which is computationally efficient for the oblique stripe removal. However, these methods must pre-establish the reference histogram, which is usually not easy to obtain. In addition, filtering-based and histogram-based methods focused on directly estimating the clear image from the observed image, and the resulting image is either over-smooth or contains residual stripe noise. Recently, Chang et al. [12] proposed a transformed low-rank model for line pattern noise removal, whose main idea was to rotate the oblique noise into a vertical form, so that the low-rankness prior was applicable. More precisely, they first rotated the image into a larger domain to perform destriping, then extracted the center part of the result and interpolated it to the original image size. However, the extraction and interpolation operators unavoidably damage the high-frequency information in the resulting image.

In order to avoid the loss of high-frequency information, we propose a novel sheared decomposition framework for oblique stripe removal, in which the stripe and image components are characterized by appropriate priors. The main idea is to perform a shear operation on the observed image so that the oblique stripe is transformed to nearly vertical lines. In the sheared domain, we observe that the stripe component exhibits obvious low-rankness and group sparsity structure. In addition, when the stripe is vertical, the stripe component changes the statistical distribution of horizontal derivation obviously, while the vertical derivation changes less. Based on the above observations, we employ low-rankness and group sparsity regularizations to characterize the stripe component, and utilize UTV to characterize the smoothness prior of the image component for destriping. To tackle the proposed model efficiently, we develop an alternating direction method of multipliers (ADMM) [4,20] algorithm with guaranteed convergence. Experimental results on simulated and real data show better destriping performance of the proposed method by comparing with the state-of-the-art destriping methods. The main contributions of the proposed method are summarized as follows:

• We propose a novel sheared destriping model to effectively exploit the directional characteristic, low-rankness, and group sparsity of the oblique stripe in a unified manner.

• We develop the ADMM algorithm to solve the proposed model, and the convergence of the algorithm is theoretically guaranteed.

• Experimental results on simulated and real data demonstrate that the proposed method outperforms the state-of-the-art methods.

The rest of this paper is organized as follows. The proposed model and its optimization procedure are formulated in Section 2. Simulated and real data experiments are described in Section 3. Finally, we conclude this paper in Section 4.

2. The proposed model

In this section, we give the proposed model and analyze the motivation of each term. Section 2.1 introduces a sheared degradation model. Section 2.2 gives a sheared low-rankness recovery model and analyzes the motivation of each term. Finally, the proposed model is solved in Section 2.3.
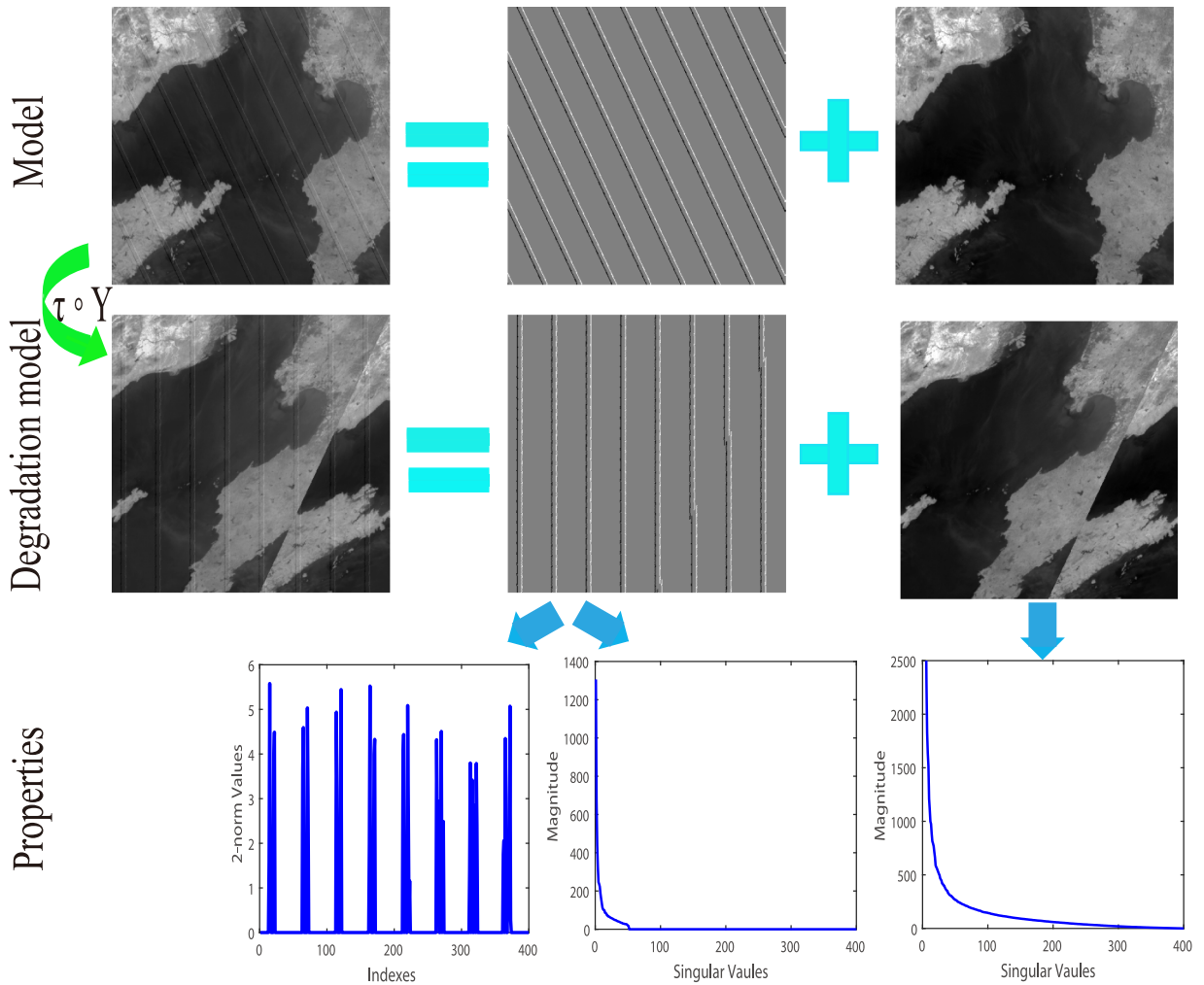
2.1. The sheared degradation model

The degradation model of remote sensing imagery can be formulated as follows:

$$Y = U + S + N,$$

where Y, U, S, and $N \in \mathbb{R}^{M \times N}$ are the degraded image, the potential clear image, the additive oblique stripe noise, and the Gaussian noise, respectively. In order to directly use low-rankness regularization to depict the distinct direction characteristic of the line pattern noise, Chang et al. [12] proposed a transformed low-rank model by rotating the observed image vertically, which reduces the high-frequency information of the original image.

In order to overcome the shortcoming, we use the shear operator to transform the oblique stripe noise vertically (shown in Fig. 1), which does not include rotation and filling up. This shear operation helps to transform oblique stripes into vertical ones by changing the relative positions of different rows. Where the operator τ [34] is determined by the parameters α, and

Fig. 1. Overview of the proposed method. In the first row, the degradation model of remote sensing imagery. In the second row, the input image is sheared to the domain where the stripe noise has strictly vertical appearance. In the third row, the stripe layer has distinct properties.

α is used to control the shear angle (see [34] for more details). In our paper, the steps of determining the shear operator τ are listed as follows:

• Generally, the angle between the vertical direction and the oblique stripe distributes in $(-\frac{\pi}{2}, \frac{\pi}{2}]$. If the angle belongs to $(-\frac{\pi}{2}, 0)$, we can restrict it into the range of $(0, \frac{\pi}{2})$ by the left-right flipping. If the angle belongs to $(\frac{\pi}{4}, \frac{\pi}{2}]$, we can restrict it into the range of $[0, \frac{\pi}{4})$ by transposing (i.e. interchanging the rows and columns of a given matrix). Thus, to save space, we only discuss the situations where $\alpha \in [0, \frac{\pi}{4})$ in the following (when the stripe is vertical, we determine the angle is zero).

• We obtain the shear angle α by the following steps: (1) performing median filtering on the observed image; (2) computing the residual image between the observed image and the filtered image; (3) performing Hough transform [2] on the residual image to calculate a rough estimation of the angle; (4) fine-tuning the angle with $[-5°, 5°]$ with the step size of $1°$.

• Given the estimated α, we apply the shear operation τ using the formula (1).

$$\tau \circ S : \mathbb{R}^{M \times N} \to \mathbb{R}^{M \times N} : S \mapsto S^\theta,$$

where the $(\bar{i}, \bar{j})$-th entry of S^θ is given, for $\bar{i} = 1, \ldots, M$ and $\bar{j} = 1, \ldots, N$, by $S^\theta_{\bar{i}, \bar{j}} := S_{i,j}$ with

$$\begin{cases} i := \bar{i}, \\ j := \left(\bar{j} - 1 + \left\lceil \frac{4}{\pi} \alpha \bar{i} \right\rceil \right) \bmod N + 1, \end{cases} \tag{1}$$

where $\lceil \cdot \rceil$ denotes the procedure of rounding the real number $\cdot$ as the nearest integer towards the direction of zero. The shear operator was first proposed in [34], for extracting texture extending in different directions in image decomposition. In our method, the shear operator can straighten the oblique stripe, so that we can directly use the low-rankness prior,
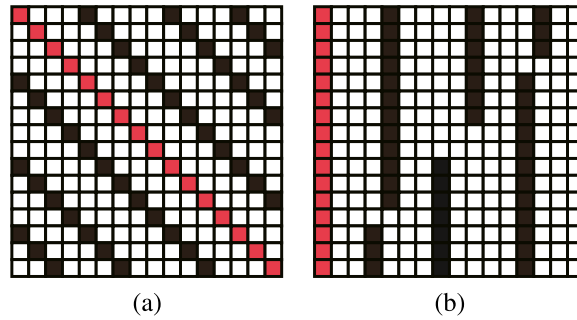
Fig. 2. An example for the shear operator (the image size is 16×16 and $\alpha = \frac{\pi}{4}$). (a) The original image; (b) The sheared image by the shear operator τ.

and the size of the output image is the same with the original image. In addition, the proposed method avoids the loss of high-frequency information since we do not perform a interpolation operator; see Fig. 1. Considering the image shown in Fig. 2(a), we can transform Fig. 2(a) into Fig. 2(b) by using the shear operator τ obtained by the above steps.

2.2. The sheared low-rank recovery model

We propose the sheared low-rank recovery model as follows:

$$\arg\min_{U,S} \frac{1}{2}\|Y - U - S\|_2^2 + \lambda_1\|\tau \circ S\|_* + \lambda_2\|\tau \circ S\|_{2,1} + \lambda_3\|\nabla_x U\|_1, \tag{2}$$

where λ_1, λ_2, and λ_3 are positive regularization parameters to balance the four terms, and $\|\tau \circ S\|_{2,1} = \Sigma_{i=1}^{N}\|(\tau \circ S)_i\|_2$, $(\tau \circ S)_i$ denotes the ith group of $\tau \circ S$. The first term in (2) is the data fidelity term. The second and third terms are the low-rankness and group sparsity regularization to characterize structure of the stripe component, respectively. The fourth term is the UTV regularization to characterize the image layer. In the following, we explain all the regularizations in our model in detail.

The low-rankness of the oblique stripe component. We use the low-rankness property of the sheared domain to characterize the distinctly directional property of the oblique stripe. In Fig. 1, we see that the singular values show different sparsity degrees, and the singular values of the sheared oblique stripe decrease to zero much rapidly. Thus, we argue that the low-rankness property of the sheared domain of the oblique stripe component is much superior. The above results motivate us to use the low-rankness prior on the sheared oblique stripe directly, i.e., $R_1(s) = \|\tau \circ S\|_*$.
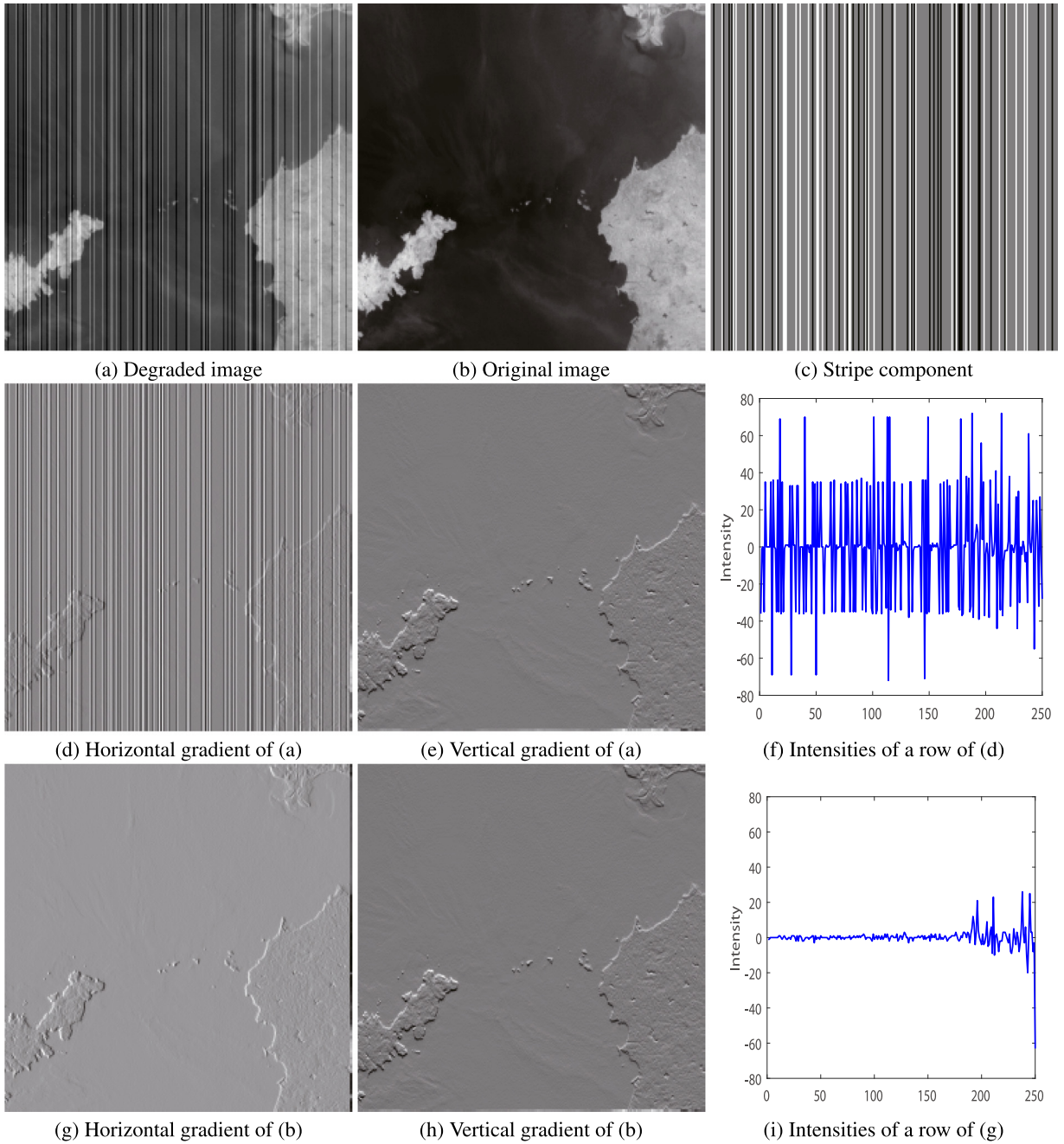
The group sparsity of the oblique stripe component. Fig. 1 shows the group sparsity of the sheared oblique stripe. To further explore the properties of the stripe component, we plot the histogram with the horizontal axis to represent the number of columns and the vertical axis to represent the 2-norm for each column of the stripe component. It shows that the ordinate values in stripe-free are very small, and the reason is that the pixel value is zero at the stripe-free location. In fact, the sheared oblique stripe has the obvious group column sparsity structure. Based on the above conclusion, we use the group sparsity structure to constrain the stripe component, i.e., $R_2(s) = \|\tau \circ S\|_{2,1}$.

The smoothness of the image component. A significant feature of the natural image is smoothness in the sense which means that the values between adjacent pixels change a little. This suggests us to describe the properties of the image layer by using the sparsity in the derivative domain. Fig. 3 presents the directional derivations of the degraded image and original image when the stripe angle is zero (i.e., the stripe is vertical). When the stripe is vertical, the stripe seriously destroys the derivative variation across the stripe line direction (the horizontal direction) while has less influence along the stripe line. Furthermore, compared with the intensities of a random row in Fig. 3(f) and (i), we find that the stripe mainly damages the sparseness of the horizontal derivation of original image. Based on this phenomenon, we only use UTV in horizontal derivation to characterize the image layer. More specifically, the regularization term for the image component is designed as $R_3(u) = \|\nabla_x U\|_1$.

2.3. ADMM optimization algorithm

It is difficult to directly solve S and U from (2) since the regularization terms are nondifferentiable and inseparable. To overcome this problem, we utilize the alternating direction method of multipliers (ADMM) to solve the proposed model, and the convergence of this algorithm is theoretically guaranteed [4,20,32]. First, by introducing three auxiliary variables $D = \tau \circ S$, $Q = \tau \circ S$, and $V = \nabla_x U$, we convert the unconstrained minimization problem (2) into the following constrained one:

$$\arg\min_{U,S,D,Q,V} \frac{1}{2}\|Y - U - S\|_F^2 + \lambda_1\|D\|_* + \lambda_2\|Q\|_{2,1} + \lambda_3\|V\|_1,$$

$$\text{s.t. } \tau \circ S = D, \ \tau \circ S = Q, \ \nabla_x U = V, \tag{3}$$

(a) Degraded image   (b) Original image   (c) Stripe component

(d) Horizontal gradient of (a)   (e) Vertical gradient of (a)   (f) Intensities of a row of (d)

(g) Horizontal gradient of (b)   (h) Vertical gradient of (b)   (i) Intensities of a row of (g)

Fig. 3. The directional gradients for the degraded image and original image. This figure shows that the stripes only affect the horizontal gradient of the desired image.

the corresponding augmented Lagrangian as follows:

$$L(D, Q, V, U, S, P) = \frac{1}{2}\|Y - U - S\|_F^2 + \lambda_1\|D\|_* + \lambda_2\|Q\|_{2,1} + \lambda_3\|V\|_1$$

$$+ \frac{\beta_1}{2}\|\tau \circ S - D + \frac{P_1}{\beta_1}\|_F^2 + \frac{\beta_2}{2}\|\tau \circ S - Q + \frac{P_2}{\beta_2}\|_F^2 + \frac{\beta_3}{2}\|\nabla_x U - V + \frac{P_3}{\beta_3}\|_F^2, \tag{4}$$

where P_1, P_2, and P_3 denote the Lagrange multipliers and β_1, β_2, and β_3 are positive penalty parameters. Then ADMM iterates as follows:

$$
\begin{cases}
(D^{l+1}, Q^{l+1}, V^{l+1}) = \underset{D,Q,V}{\arg\min}\, L(S^l, U^l, D, Q, V, P_1^l, P_2^l, P_3^l), \\
(U^{l+1}, S^{l+1}) = \underset{S,U}{\arg\min}\, L(S, U, D^{l+1}, Q^{l+1}, V^{l+1}, P_1^l, P_2^l, P_3^l), \\
P_1^{k+1} = P_1^k + \beta_1(\tau \circ S^{k+1} - D^{k+1}), \\
P_2^{k+1} = P_2^k + \beta_2(\tau \circ S^{k+1} - Q^{k+1}), \\
P_3^{k+1} = P_3^k + \beta_3(\nabla_x U^{k+1} - V^{k+1}).
\end{cases}
$$

Below we give the details of solving each subproblem.

• In step one, we solve variables D, Q, and V. Since they are decoupled, their optimal solutions can be calculated separately.

(1) The D-subproblem is

$$
D^{k+1} = \underset{D}{\arg\min}\, \lambda_1 \|D\|_* + \frac{\beta_1}{2}\|\tau \circ S - D + \frac{P_1}{\beta_1}\|_F^2,
$$

which is a typical low-rank matrix approximation problem and has a closed-form solution [5]. It can be efficiently solved by the following singular value thresholding operation:

$$
\begin{cases}
D^{k+1} = U^k(\mathrm{shrink}_*(\Sigma, \lambda))(V^k)^T, \\
\mathrm{shrink}_*(\Sigma, \lambda) = \max\left(\Sigma_{ii} - \frac{\lambda_1}{\beta_1}, 0\right),
\end{cases}
\tag{5}
$$

where $\tau \circ S^k + \frac{P_1^k}{\beta_1} = U^k \Sigma(V^k)^T$ is the singular value decomposition of $\tau \circ S^k + \frac{P_1^k}{\beta_1}$ and Σ_{ii} is the diagonal element of the singular value matrix Σ.

(2) The Q-subproblem is

$$
Q^{k+1} = \underset{Q}{\arg\min}\, \lambda_2 \|Q\|_{2,1} + \frac{\beta_2}{2}\|\tau \circ S - D + \frac{P_2}{\beta_2}\|_F^2,
$$

which has a closed-form solution by the following soft-shrinkage formula [51]:

$$
Q_{g_i}^{k+1} = \max\left\{\|r_i\|_2 - \frac{\lambda_2}{\beta_2}, 0\right\}\frac{r_i}{\|r_i\|_2}, \quad r_i = (\tau \circ S^k)_{g_i} + \frac{1}{\beta_2}(P_2^k)_{g_i},
\tag{6}
$$

where g_i denotes each group of the image.

(3) The V-subproblem is

$$
V^{k+1} = \underset{V}{\arg\min}\, \lambda_3 \|V\|_1 + \frac{\beta_3}{2}\|\nabla_x U - V + \frac{P_3}{\beta_3}\|_F^2,
$$

which can be efficiently solved by the following soft-threshold shrinkage operation [19]:

$$
V^{k+1} = \mathrm{shrink}\left(\nabla_x U^k + \frac{P_3^k}{\beta_3}, \frac{\lambda_3}{\beta_3}\right),
\tag{7}
$$

where

$$
(\mathrm{shrink}(A, \xi))_{i,j} = \frac{A_{i,j}}{|A_{i,j}|} * \max(|A_{i,j}| - \xi, 0),
$$

and the convention $0 \cdot \frac{0}{0}$ is assumed.

• In step two, the (U, S)-subproblem is a least squares problem given by

$$
(U^{k+1}, S^{k+1}) = \underset{U,S}{\arg\min}\, \frac{1}{2}\|Y - U - S\|_F^2 + \frac{\beta_1}{2}\|\tau \circ S - D + \frac{P_1}{\beta_1}\|_F^2
$$
$$
+ \frac{\beta_2}{2}\|\tau \circ S - Q + \frac{P_2}{\beta_2}\|_F^2 + + \frac{\beta_3}{2}\|\nabla_x U - V + \frac{P_3}{\beta_3}\|_F^2,
$$

and the corresponding solution can be obtained by solving the normal equation as follows:

$$
\begin{pmatrix} A_1 & I \\ I & A_2 \end{pmatrix}\begin{pmatrix} U \\ S \end{pmatrix} = \begin{pmatrix} B_1 \\ B_2 \end{pmatrix},
\tag{8}
$$

where $A_1 = I + \beta_3 \nabla_x^T \nabla_x$, $A_2 = I + \beta_1 + \beta_2$, $B_1 = Y + \beta_3 \nabla_x^T (V^{k+1} - \frac{P_3^k}{\beta_3})$, and $B_2 = Y + \beta_1(\tau^{-1} \circ D^{k+1} - \tau^{-1} \circ \frac{P_1^k}{\beta_1}) + \beta_2(\tau^{-1} \circ Q^{k+1} - \tau^{-1} \circ \frac{P_2^k}{\beta_2})$, as ∇_x is a first-order difference matrix, $\nabla_x^T \nabla_x$ can be diagonalized by the transform matrix Φ, i.e., $\nabla_x^T \nabla_x = \Phi^T \Lambda_1 \Phi$ [53]. For a detailed discussion, we obtain the following decomposition:

$$\begin{pmatrix} A_1 & I \\ I & A_2 \end{pmatrix} = \begin{pmatrix} \Phi^T & 0 \\ 0 & \Phi^T \end{pmatrix} \begin{pmatrix} I + \beta_3 \Lambda_1 & I \\ I & A_2 \end{pmatrix} \begin{pmatrix} \Phi & 0 \\ 0 & \Phi \end{pmatrix},$$

and the normal equations can be solved by using fast transforms (FFT).

• In step three, we update the lagrange multipliers P_1, P_2, and P_3 as follows:

$$\begin{cases} P_1^{k+1} = P_1^k + \beta_1(\tau \circ S^{k+1} - D^{k+1}), \\ P_2^{k+1} = P_2^k + \beta_2(\tau \circ S^{k+1} - Q^{k+1}), \\ P_3^{k+1} = P_3^k + \beta_3(\nabla_x U^{k+1} - V^{k+1}). \end{cases} \tag{9}$$

Although there are five components in the constrained problem (3), they can be categorized as two parts. Let

$$H = \begin{pmatrix} D \\ Q \\ V \end{pmatrix}, G = \begin{pmatrix} U \\ S \end{pmatrix}.$$

The optimization problem (4) is well structured since all the variable can be separated into two groups, which are H and G. Due to the variables D, Q and V are decoupled and the convexity of the quadratic norm, which satisfy the framework of ADMM [4,20]. Based on the previous derivation, we develop the following ADMM iterative scheme for the model (2), as outlined in Algorithm 1.

Algorithm 1 The sheared low-rank destriping algorithm.

Input: observed image **Y**, parameters λ_1, λ_2, λ_3, β_1, β_2, β_3, and $\varepsilon = 10^{-4}$.
1: Initialize: $\mathbf{S}^0 = \mathbf{U}^0 = \mathbf{D}^0 = \mathbf{Q}^0 = \mathbf{V}^0 = \mathbf{0}$, and $\mathbf{P}_1 = \mathbf{P}_2 = \mathbf{P}_3 = \mathbf{0}$.
2: **while** not converged ($\|(\mathbf{U}^\theta)^{k+1} - (\mathbf{U}^\theta)^k\|_F / \|(\mathbf{U}^\theta)^k\|_F < \varepsilon$) **do**
3:       Update $\mathbf{D}^{k+1}$, $\mathbf{Q}^{k+1}$, $\mathbf{V}^{k+1}$ via (5), (6), and (7);
3:       Update $\mathbf{S}^{k+1}$ and $\mathbf{U}^{k+1}$, via (8);
4:       Update the multiplier $\mathbf{P}_1^{k+1}$, $\mathbf{P}_2^{k+1}$, and $\mathbf{P}_3^{k+1}$ via (9);
5: **end while**
**Output: U**.

---

3. Experimental results

In this section, we give experimental results to test the performance of the proposed method. Section 3.1 gives the experimental settings. Sections 3.2 and 3.3 test the proposed method using the simulated and the real data, respectively. Some discussions are given in Section 3.4.

3.1. Experimental setting

We compare the proposed method with the state-of-the-art destriping methods, including low-rank-based single-image decomposition model (denoted as LRSID) [11], UTV model (denoted as UTV) [3], low-pass filtering (denoted as LF) method [18], and median filtering (denoted as MF) method [39]. All experiments are run in MATLAB (R2016b) on a desktop of 2 GB RAM, Inter (R) Core (TM) i3-3240 CPU @3.40 GHz.

Stripe noise generation. For convenience of the parameter selection, the pixel values of the simulated and real data are normalized to [0,1]. We denote the stripe level using a vector with two elements, e.g., (intensity, percentage), where 'intensity' denotes the absolute value of pixels of each stripe line and 'percentage' (denote as r) represents the percentage of the stripe area within the image. In our simulation experiments, the intensity is in the set of {10, 30, 50}, and r is in the set of {0.1, 0.2, 0.3}. We select $r \times n$ lines in the image to add the stripe for the simulating case. The absolute value of each pixel of each line is the same.

Evaluation indices. We use several qualitative and quantitative assessments to evaluate the destriping performance. Qualitative indices include the visual impact and the mean cross-track profile. Mean cross-track profile is a table, where the x-axis and the y-axis represent the column number of the image and the mean value of each column, respectively. We use two objective quantitative indices: the peak signal-to-noise ratio (PSNR) and the structural similarity (SSIM) [47] to

| (a) | (b) | (c) 32.10, 0.968 | (d) 35.44, 0.987 | (e) **41.68**, **0.992** |
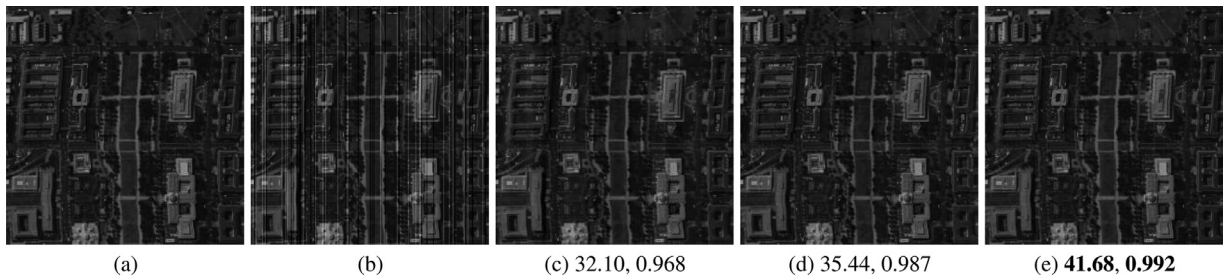
Fig. 4. The destriping results with the simulated nonperiodic stripe case (the corresponding PSNR (dB) and SSIM values are given under (c)–(e)). (a) The original hyperspectral image; (b) The degraded image; The destriping results by (c) LRSID, (d) UTV, and (e) the proposed method.

evaluate the performance, which are defined as follows:

$$\text{PSNR} = 10 \ \log_{10} \ \frac{mn(\text{Max}_U)^2}{\|U - U^*\|_F^2},$$

$$\text{SSIM} = \frac{(2\mu_U \cdot \mu_{U^*} + c_1)(2\sigma_{UU^*} + c_2)}{(\mu_U^2 + \mu_{U^*}^2 + c_1)(\sigma_U^2 + \sigma_{U^*}^2 + c_2)},$$

where U is the recovered image, U^* is the true image, Max_U is the maximum pixel of U, μ_U and μ_{U^*} are the mean values of U and U^*, σ_{UU^*} is the covariance of U and U^*, σ_U and σ_{U^*} are the standard variances of U and U^*, respectively, and $c_1, c_2 > 0$ are constants. In general, higher PSNR and SSIM indices indicate better destriping performance. For the real experimental data, since the ground-truth image is unavailable, we choose no-reference evaluation indices noise reduction (NR) [3,9,38], and mean relative deviation (MRD) [9,38] to evaluate the performance of the proposed method. NR is used to assess the ratio of stripe noise reduction in the frequency domain, and MRD is used to evaluate the performance of maintaining the original pixel in the remote sensing imagery. It is noteworthy that reasonable NR values and lower MRD values mean better quantitation results. For qualitative evaluation, we use the mean cross-track profile and power spectrum.

Parameters selection. The proposed method involves three regularization parameters λ_1, λ_2, and λ_3, which determine the degree of stripe removal. According to the dense level of the stripe component in the test image, we empirically run the balance parameters in (2) λ_1, λ_2, and λ_3 within [0.001, 0.1], [0.0001, 0.01], and [0.0001, 0.01] with increment of 0.0001, and penalty parameters in (4) run $\beta_1 = \beta_2 = \beta_3 = 1$. We will discuss the selections of λ_1, λ_2, and λ_3 in Section 3.4. We try our best to adjust the parameters of the compared methods to obtain the best results according to the authors' suggestion.

3.2. Simulated experiments

In this section, we test the proposed method in two stripe cases: adding vertical stripes to a hyperspectral subimage of Washington DC Mall[1] of size 256×256, and adding oblique stripes to the MODIS image[2] band 32 of size 400×400.

3.2.1. The vertical stripe case
We randomly add twenty percent of the non-periodic stripe into a 256×256 hyperspectral subimage. The pixels absolute value of the stripe line is 50, and the noise intensity of each stripe line is equal.

Fig. 4 shows the destriping results by different methods. We can see that LRSID and UTV remove most of stripe, but the image structure in the same direction as the stripe are suppressed and some residual stripe cannot be removed. As comparison, the proposed method has the best destriping results for removing stripe and preserving image details; see Fig. 4(e).

Fig. 5 shows the estimated stripe images by different methods and compares the estimated stripe among three methods with the original stripe. In Fig. 5(d), the vertical and horizontal axes represent the mean value of each stripe line and the column number, respectively. We can find that UTV and LRSID fail to precisely estimate the stripe component and create some minor errors in the stripe-free regions. However, destriping results by the proposed method can be closer to the zero values in stripe-free regions and precisely estimate the stripe component.

Fig. 6 shows the average of each column of the destriping results compared with the original image. The vertical and horizontal axes represent the mean of each column and the column number, respectively. We can see that the destriping results by UTV and LRSID exist some residual stripe. In comparison, the proposed method performs the best and has same curve with the original image profile.

The values below Fig. 4 represent PSNR and SSIM results for the three destriping methods in simulated data experiments. From which, we can observe that the proposed method has better PSNR and SSIM results in the simulated experiments, which further indicates that the proposed method outperforms the other two methods.
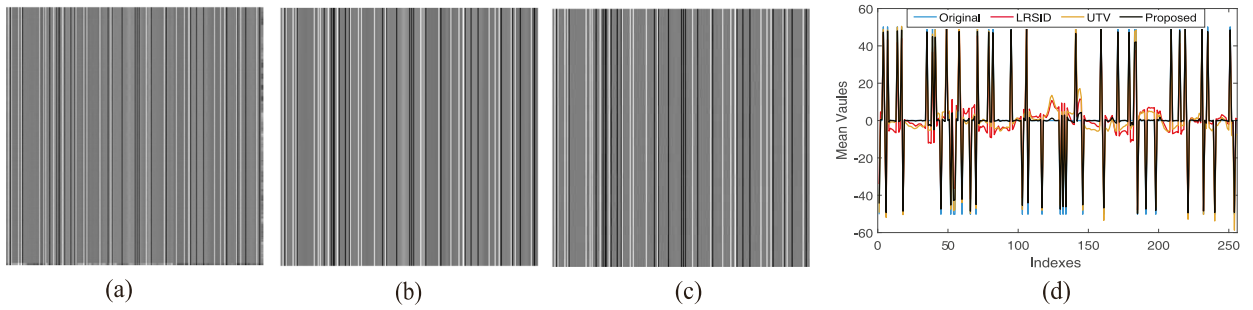

Fig. 5. The estimated stripes by (a) LRSID, (b) UTV, and (c) the proposed method of Fig. 4; (d) The mean value comparison between the stripe estimated by LRSID, UTV, the proposed method, and the original one.
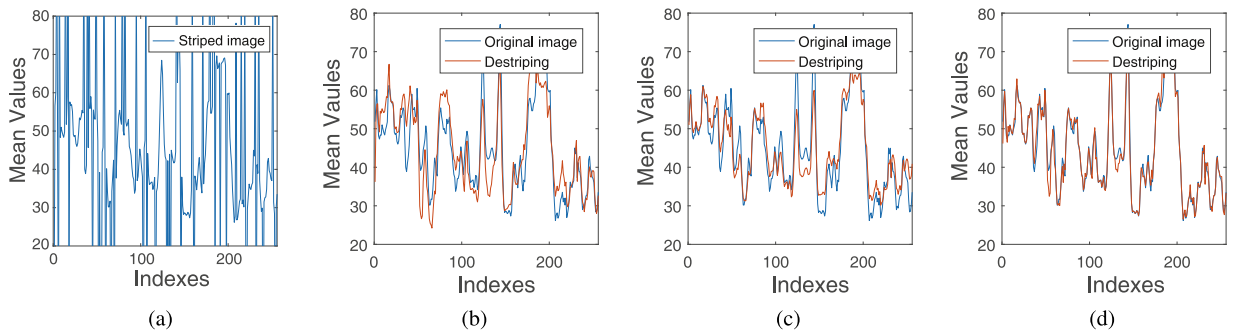

Fig. 6. Column mean cross-track profiles of Fig. 4. (a) The striped image; (b) LRSID; (c) UTV; (d) The proposed method.
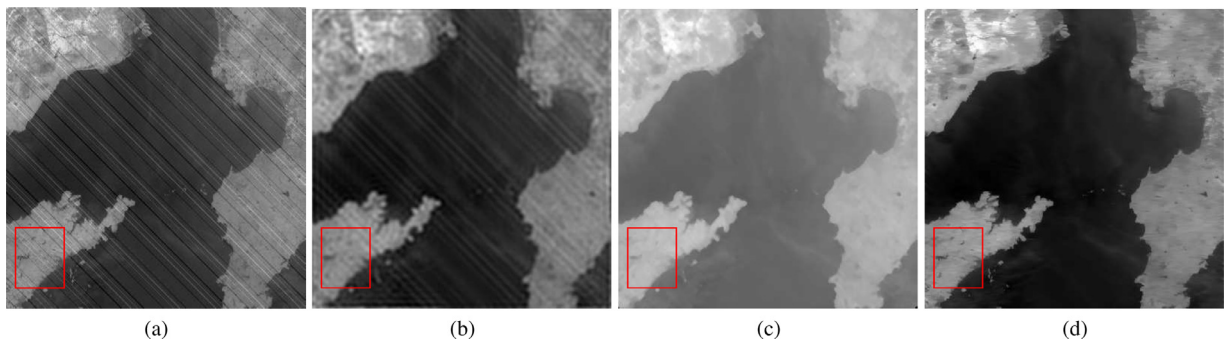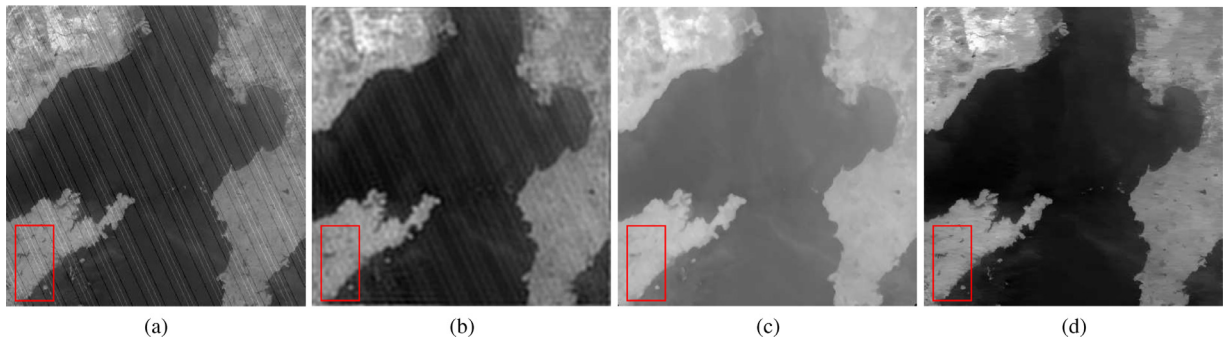

Fig. 7. The removal results at an angle of 45. (a) The observed image; The destriping results by (b) LF, (c) MF, and (d) the proposed method.

3.2.2. The oblique stripe case

Here, we compare the proposed method with LF and MF. We add periodic and nonperiodic stripe in a 400×400 MODIS image with different angles. The absolute value of each pixel of each line is the same.

Figs. 7 and 8 show the destriping results of the three methods with different angles. Regarding visual effects, we can observe that the destriping results obtained by LF show some residual stripe. While those by MF show that all stripe can be removed completely, but the restored image is blurred. Destriping results by the proposed method as shown in Figs. 7(d) and 8(d) are better than those of the other two comparing methods in preserving the stripe-free information and suppressing artifacts.

Tables 1 and 2 show the PSNR and SSIM results for the three destriping methods in different situations, where 'intensity' denotes the absolute value of pixels of each stripe line and 'percentage' (denote as r) represents the percentage of the stripe area within the image. From Tables 1 and 2, we can observe that the proposed method obtains better PSNR and SSIM values in the simulation experiments. Combined with the visual effects discussed before, we can conclude that the quantitative assessment results are consistent with the visual effects.

Fig. 8. The removal results at an angle of 25. (a) The observed image; The destriping results by (b) LF, (c) MF, and (d) the proposed method.

Table 1
PSNR (dB) and SSIM results of the test methods for different stripe noise types at an angle of 45.

Stripe	Method	Index	r = 0.1			r = 0.2			r = 0.3		
			Intensity			Intensity			Intensity		
			10	30	50	10	30	50	10	30	50
	LF	PSNR	35.73	31.04	28.79	34.16	28.46	25.54	33.34	26.90	23.39
		SSIM	0.916	0.844	0.814	0.881	0.780	0.803	0.878	0.802	0.783
periodic	MF	PSNR	34.37	34.03	33.81	32.70	31.14	30.70	30.67	29.10	27.11
		SSIM	0.904	0.901	0.900	0.876	0.853	0.850	0.845	0.825	0.815
	Ours	PSNR	**47.05**	**42.25**	**39.40**	**41.59**	**36.69**	**34.91**	**39.42**	**32.52**	**29.42**
		SSIM	**0.992**	**0.986**	**0.972**	**0.982**	**0.966**	**0.950**	**0.983**	**0.951**	**0.922**
	LF	PSNR	35.63	30.38	27.94	34.18	27.84	24.47	33.45	26.67	23.16
		SSIM	0.916	0.844	0.814	0.881	0.780	0.803	0.878	0.802	0.783
nonperiodic	MF	PSNR	32.82	32.57	30.01	30.13	29.67	29.16	29.95	27.83	25.81
		SSIM	0.988	0.876	0.876	0.840	0.833	0.829	0.839	0.812	0.794
	Ours	PSNR	**45.14**	**39.99**	**38.26**	**41.90**	**35.89**	**33.41**	**39.18**	**31.37**	**28.14**
		SSIM	**0.989**	**0.972**	**0.961**	**0.985**	**0.965**	**0.936**	**0.984**	**0.959**	**0.920**

Table 2
PSNR (dB) and SSIM results of the test methods for different stripe noise types at an angle of 25.

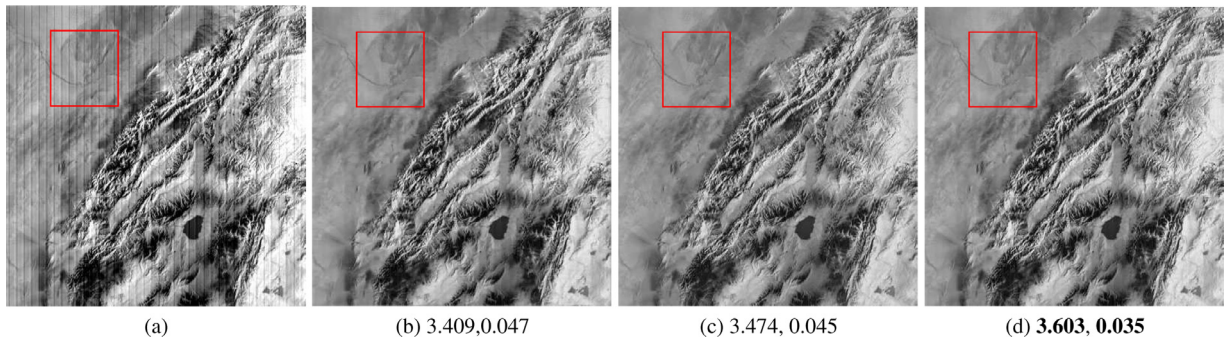| Stripe	Method	Index	r = 0.1			r = 0.2			r = 0.3		
			Intensity			Intensity			Intensity		
			10	30	50	10	30	50	10	30	50
	LF	PSNR	35.83	31.26	29.19	34.30	28.67	31.60	33.44	27.10	23.54
		SSIM	0.918	0.852	0.838	0.884	0.803	0.825	0.880	0.828	0.803
periodic	MF	PSNR	37.27	34.15	33.99	32.71	32.07	31.60	31.51	30.42	28.97
		SSIM	0.943	0.903	0.902	0.876	0.870	0.866	0.858	0.845	0.827
	Ours	PSNR	**45.72**	**40.02**	**37.56**	**41.91**	**36.09**	**33.38**	**39.39**	**32.57**	**28.98**
		SSIM	**0.988**	**0.963**	**0.944**	**0.980**	**0.949**	**0.924**	**0.976**	**0.934**	**0.874**
	LF	PSNR	35.75	30.52	28.15	34.30	27.96	24.67	33.28	26.31	24.67
		SSIM	0.918	0.852	0.838	0.884	0.803	0.825	0.880	0.828	0.803
nonperiodic	MF	PSNR	34.29	31.61	30.64	30.81	30.19	29.21	29.91	27.52	29.21
		SSIM	0.904	0.859	0.846	0.847	0.834	0.830	0.839	0.811	0.830
	Ours	PSNR	**44.78**	**38.78**	**36.63**	**41.45**	**35.78**	**33.57**	**398.42**	**30.95**	**33.60**
		SSIM	**0.987**	**0.962**	**0.945**	**0.981**	**0.949**	**0.924**	**0.978**	**0.939**	**0.924**

3.3. Real experiments

In this section, we choose three representative applications: the Aqua MODIS image[2], the Terra MODIS image[3] and the Landsat 7[4] image obtained by Landsat 8[5] geo-registration. We use these stripe noise removal tasks to validate the effectiveness of the proposed method. For convenience of discussion, the gray values of each stripe image are scaled into the interval [0,1].
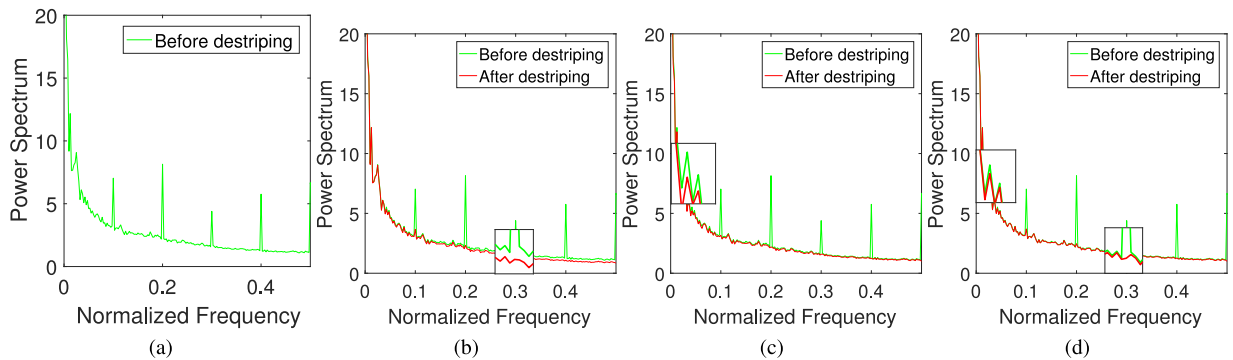
---

[3] https://ladsweb.nascom.nasa.gov/
[4] https://landsat.usgs.gov/landsat-7-data-users-handbook-section-5
[5] https://landsat.usgs.gov/landsat-8-l8-data-users-handbook

(a)   (b) 3.409,0.047   (c) 3.474, 0.045   (d) **3.603**, **0.035**

Fig. 9. (a) The observed image; The destriping results by (b) LRSID, (c) UTV, and (d) the proposed method (the corresponding NR and MRD values are given under (b)–(d)).

(a)   (b)   (c)   (d)

Fig. 10. Power spectrums of Fig. 9. (a) The original image; (b) LRSID; (c) UTV; and (d) the proposed method.

Table 3
NR and MRD comparison of Figs. 11 and 12.

| Image	Terra MODIS			Landsat 7		
Method	LF	MF	Ours	LF	MF	Ours
NR	1.303	1.668	**2.492**	1.367	1.962	**2.134**
MRD	0.106	0.118	**0.100**	0.655	0.056	**0.035**

3.3.1. The vertical stripe case

Fig. 9 shows the recovered results by three methods. We can see that the destriping result by LRSID shows some residual stripe, while the destriping result by UTV shows that all the stripe can be removed completely, but some regions are blurred. Destriping result by the proposed method is shown in Fig. 9(d), which is better than the other two comparing methods in preserving the stripe-free information and suppressing artifacts.

We show the power spectrum of the Aqua MODIS in Fig. 10, in order to illustrate the experimental results vividly. The vertical and horizontal axes represent the normalized frequency and the mean power spectrum of all row, respectively. In Fig. 10(a), there are several large impulses in curve due to the effects of stripe, while the original ground-truth image exhibits the smoother curve. From Fig. 10(b) and (c), the sharp impulse of curves become smooth, but in the other positions, the mean power spectrum of the destriping results curve show most of the burrs compared with the observed image power spectrum one.

The values below Fig. 9 shows the quantitation indices NR and MRD results for the three destriping methods. From which, we can observe that the proposed method has better NR and MRD results than the comparing destriping methods.

3.3.2. The oblique stripe case

Figs. 11 and 12 show the final destriping results, they are obtained by considering visual effects and the spectral features. Fig. 11(a) is an oblique stripe image rotated by a real Terra MODIS vertical stripe image, and Fig. 12(a) is a Landsat 7 oblique stripe image obtained by Landsat 8 geo-registration. Figs. 11(b)–(c) and 12(b)–(c) show the clear reduction of the stripe; however, the image are blurred. On the contrary, the proposed method not only removes a lot of stripe but also retains most information of the stripe-free regions. Table 3 shows the quantitation indices NR and MRD results for the three destriping methods. From Table 3, we can observe that the proposed method has better NR and MRD results than the comparing destriping methods, which further indicates that the proposed method outperforms the other two methods.
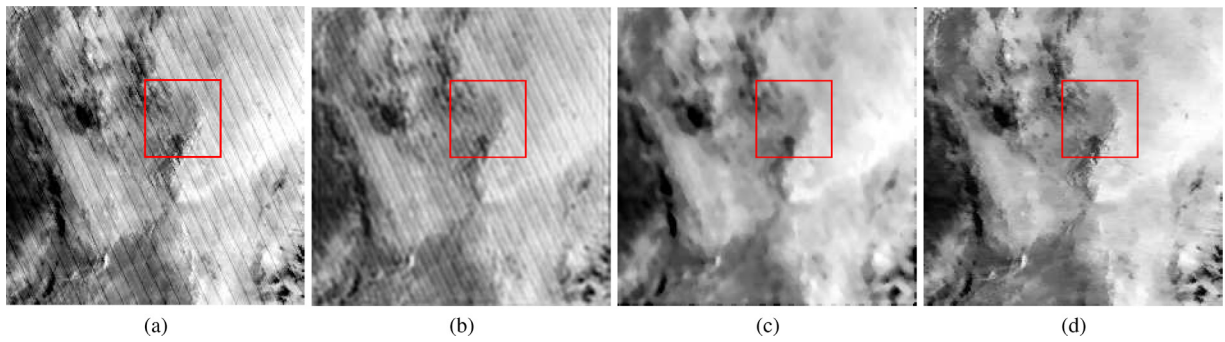
Fig. 11. (a) The observed image; The destriping results by (b) LF, (c) MF, and (d) the proposed method.
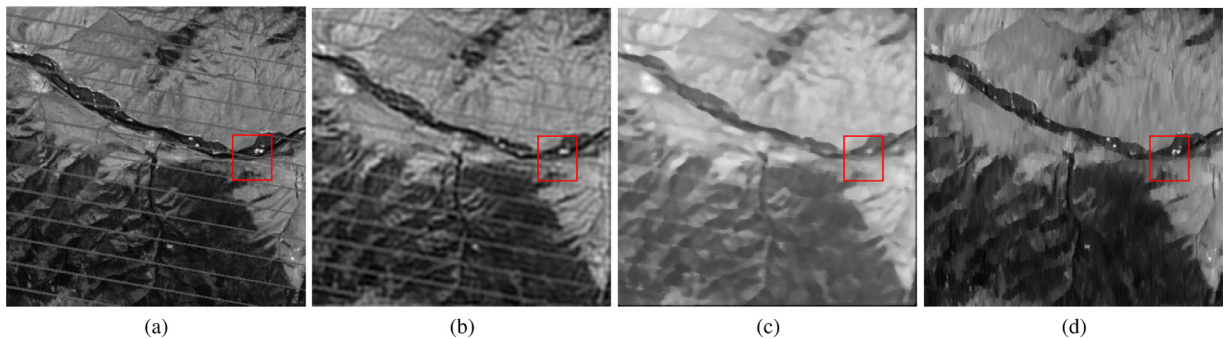
Fig. 12. (a) The observed image; The destriping results by (b) LF, (c) MF, and (d) the proposed method.
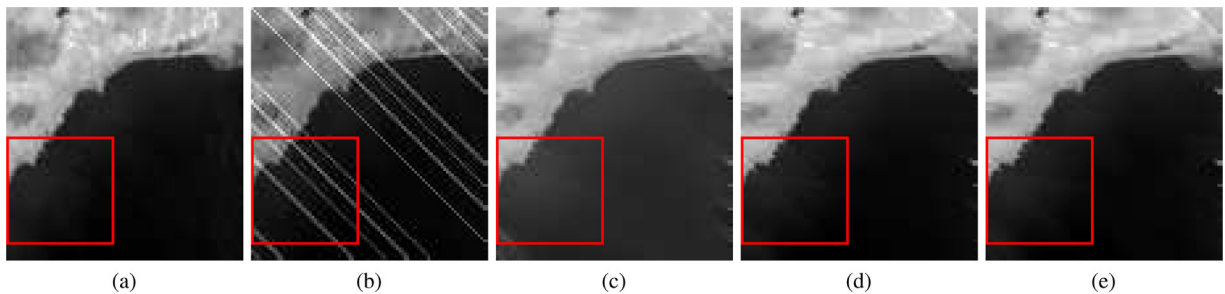

Fig. 13. Effectiveness of the proposed method (the stripe noise at an angle of 45, r = 0.1, intensity = 50). (a) The original image (PSNR, SSIM); (b) Observed image (23.96, 0.53); (c) The proposed method without the group sparsity (32.63, 0.93); (d)The proposed method without the low-rankness (36.75, 0.96); (e) The proposed method (37.05, 0.96).

3.4. Discussion

Regularization terms analysis. In our method, we use the low-rankness and group sparsity regularization to capture the characteristics of stripes noise. To illustrate why their combination is better for the final performance, we show different settings of regularization terms in Fig. 13. Compared with Fig. 13(c) and (e), there are many obvious blurring effects in Fig. 13(c), it demonstrates that the group sparsity is necessary to keep the sharpness of the image and exclude stripes noise. Compared with Fig. 13(d) and (e), Fig. 13(e) contains a lot of details, which proves that the low-rankness of stripes noise is useful for the proposed method. Therefore, by combining UTV, low-rankness, and the group sparsity constraints into the optimization problem, our method can recover the clear image.

Parameters analysis. There are three regularization parameters involved in our model (2): λ_1, λ_2, and λ_3. To verify the robustness of regularization parameters, we give a sensitivity analysis by using simulated experiment periodical stripe Fig. 7 as an example and using the PSNR values as the evaluation measure. The best way to select the optimal value of these three parameters is to find the global optimal value of PSNR in the three-dimensional parameters space. However, this will unavoidably need a lot of time and computation. To overcome this difficulty, we use a greedy strategy to select the parameter values one by one. Fig. 14 plots the curves of the PSNR values as a function of the regularization parameters λ_1, λ_2, and λ_3. From Fig. 14, we can observe that PSNR performs obvious improvement when λ_1 is increased from 0 to 0.02.
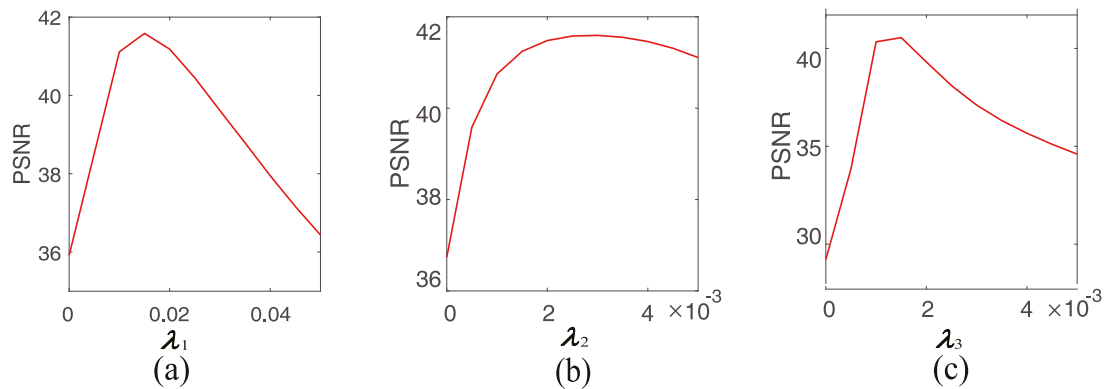
Fig. 14. PSNR curves as function of the regularization parameters. (a) The relationship between PSNR and λ_1 ($\lambda_2 = 0.005, \lambda_3 = 0.001$); (b) The relationship between PSNR and λ_2 ($\lambda_1 = 0.02, \lambda_3 = 0.001$); (c) The relationship between PSNR and λ_3 ($\lambda_1 = 0.02, \lambda_2 = 0.005$).

Moreover, we also observe that PSNR appears a fast reduction when λ_1 further increasing. In general, the highest PSNR values is achieved with λ_1 in 0.02. And the similar observation can be obtained with the other two parameters. In our experiments, since there are extensive experiments in this paper, and the different degradation degrees of the stripe image, we empirically run λ_1, λ_2, and λ_3 within [0.005, 0.025], [0.001, 0.003], and [0.02, 0.035] with increment of 0.0001 for all the experiments.

4. Conclusions

In this work, we have proposed a novel sheared low-rank model for oblique stripe noise removal. In our model, the low-rankness and group sparsity regularization are utilized to depict the structure characteristics of the stripe component. Moreover, we characterized the smoothness image prior by UTV regularization, to preserve the strong edges and geometric features. We developed an ADMM for solving the proposed model, and the convergence of this algorithm can be guaranteed by the existing ADMM theory. Finally, the qualitative and quantitative results showed that the proposed method has better destriping performance than the state-of-the-art destriping methods, as well as preserving fine features of the original image.

Acknowledgment

References

[1] N. Acito, M. Diani, G. Corsini, Subspace-based striping noise reduction in hyperspectral images, IEEE Trans. Geosci. Remote Sens. 49 (4) (2010) 1325–1342.
[2] S. Barbarossa, Analysis of multicomponent LFM signals by a combined Wigner–Hough transform, IEEE Trans. Signal Process. 43 (6) (1995) 1511–1515.
[3] M. Bouali, S. Ladjal, Toward optimal destriping of modis data using a unidirectional variational model, IEEE Trans. Geosci. Remote Sens. 49 (8) (2011) 2924–2935.
[4] S. Boyd, N. Parikh, E. Chu, B. Peleato, J. Eckstein, Distributed optimization and statistical learning via the alternating direction method of multipliers, Found. Trends Mach. Learn. 3 (1) (2010) 1–122.
[5] J.F. Cai, E.J. Candès, Z. Shen, A singular value thresholding algorithm for matrix completion, SIAM J. Optim. 20 (4) (2010) 1956–1982.
[6] H. Carfantan, J. Idier, Statistical linear destriping of satellite-based pushbroom-type images, IEEE Trans. Geosci. Remote Sens. 48 (4) (2010) 1860–1871.
[7] Y. Chang, H. Fang, L. Yan, H. Liu, Robust destriping method with unidirectional total variation and framelet regularization, Opt. Express 21 (20) (2013) 23307–23323.
[8] Y. Chang, L. Yan, H. Fang, H. Liu, Simultaneous destriping and denoising for remote sensing images with unidirectional total variation and sparse representation, IEEE Geosci. Remote Sens. Lett. 11 (6) (2014) 1051–1055.
[9] Y. Chang, L. Yan, H. Fang, C. Luo, Anisotropic spectral-spatial total variation model for multispectral remote sensing image destriping, IEEE Trans. Image Process. 24 (6) (2015) 1852–1866.
[10] Y. Chang, L. Yan, H. Fang, S. Zhong, W. Liao, Hsi-denet: Hyperspectral image restoration via convolutional neural network, IEEE Trans. Geosci. Remote Sens. doi:10.1109/tgrs.2018.2859203.
[11] Y. Chang, L. Yan, T. Wu, S. Zhong, Remote sensing image stripe noise removal: From image decomposition perspective, IEEE Trans. Geosci. Remote Sens. 54 (12) (2016) 7018–7031.
[12] Y. Chang, L. Yan, S. Zhong, Transformed low-rank model for line pattern noise removal, IEEE Int. Conf. Comput. Vis. (2017) 1726–1734.
[13] J. Chen, H. Lin, Y. Shao, L. Yang, Oblique striping removal in remote sensing imagery based on wavelet transform, Int. J. Remote Sens. 27 (8) (2006) 1717–1723.
[14] J. Chen, Y. Shao, H. Guo, W. Wang, Destriping CMODIS data by power filtering, IEEE Trans. Geosci. Remote Sens. 41 (9) (2003) 2119–2124.
[15] Y. Chen, T.Z. Huang, L.J. Deng, X.L. Zhao, M. Wang, Group sparsity based regularization model for remote sensing image stripe noise removal, Neurocomputing 267 (6) (2017) 95–106.

[16] Y. Chen, T.Z. Huang, X.L. Zhao, Destriping of multispectral remote sensing image using low-rank tensor decomposition, IEEE J. Sel. Top. Appl. Earth Obs. Remote Sens. 11 (12) (2018) 4950–4967.

[17] Y. Chen, T.Z. Huang, X.L. Zhao, L.J. Deng, J. Huang, Stripe noise removal of remote sensing images by total variation regularization and group sparsity constraint, Remote Sens. 9 (6) (2017) 559.

[18] R.E. Crippen, A simple spatial filtering routine for the cosmetic removal of scan-line noise from landsat TM p-tape imagery, Photogr. Eng. Remote Sens. 55 (3) (1989) 327–331.

[19] D.L. Donoho, De-noising by soft-thresholding, IEEE Trans. Inf. Theory 41 (3) (2002) 613–627.

[20] J. Eckstein, D.P. Bertsekas, On the Douglas–Rachford splitting method and the proximal point algorithm for maximal monotone operators, Math. Programm. 55 (1–3) (1992) 293–318.

[21] F.L. Gadallah, F. Csillag, E.J.M. Smith, Destriping multisensor imagery with moment matching, Int. J. Remote Sens. 21 (12) (2000) 2505–2511.

[22] G. Gopalan, T.A. Govindarajan, Segmentation and classification of hyperspectral images using CHV pattern extraction grid, Soft Comput. 22 (5) (2018) 1475–1490.

[23] Z. Hamadache, Y. Smara, Oblique striping removal in EO-1 hyperspectral remote sensing imagery (2015).

[24] B.K.P. Horn, R.J. Woodham, Destriping landsat MSS images by histogram modification, Comput. Graph. Image Process. 10 (1) (1979) 69–83.

[25] J. Huang, T.Z. Huang, X.L. Deng, X.L. Zhao, Joint-sparse-blocks and low-rank representation for hyperspectral unmixing, IEEE Trans. Geosci. Remote Sens. doi:10.1109/tgrs.2018.2873326.

[26] T.Y. Ji, T.Z. Huang, X.L. Zhao, T.H. Ma, L.J. Deng, A non-convex tensor rank approximation for tensor completion, Appl. Math. Model. 48 (2017) 410–422.

[27] T.X. Jiang, T.Z. Huang, X.L. Zhao, L.J. Deng, Y. Wang, FastDeRain: a novel video rain streak removal method using directional gradient priors, IEEE Transactions on Image Processing 28 (4) (2019) 2089–2102.

[28] T.X. Jiang, T.Z. Huang, X.L. Zhao, T.Y. Ji, L.J. Deng, Matrix factorization for low-rank tensor completion using framelet prior, Inf. Sci. 436 (2018) 403–417.

[29] X. Liu, X. Lu, H. Shen, Q. Yuan, Y. Jiao, L. Zhang, Stripe noise separation and removal in remote sensing images by consideration of the global sparsity and local variational properties, IEEE Trans. Geosci. Remote Sens. 54 (5) (2016) 3049–3060.

[30] X. Lu, Y. Wang, Y. Yuan, Graph-regularized low-rank representation for destriping of hyperspectral images, IEEE Trans. Geosci. Remote Sens. 51 (7) (2013) 4009–4018.

[31] T.H. Ma, Y. Lou, T.Z. Huang, Truncated l_{1-2} models for sparse recovery and rank minimization, SIAM J. Imaging Sci. 10 (3) (2017) 1346–1380.

[32] J.J. Mei, Y. Dong, T.Z. Huang, W. Yin, Cauchy noise removal by nonconvex ADMM with convergence guarantees, J. Sci. Comput. 74 (2) (2018) 743–766.

[33] B. Münch, P. Trtik, F. Marone, M. Stampanoni, Stripe and ring artifact removal with combined wavelet–fourier filtering, Opt. Express 17 (10) (2009) 8567–8591.

[34] S. Ono, T. Miyata, I. Yamada, Cartoon-texture image decomposition using blockwise low-rank texture characterization, IEEE Trans. Image Process. 23 (3) (2014) 1128–1142.

[35] J.J. Pan, C.I. Chang, Destriping of landsat MSS images by filtering techniques, Photogramm. Eng. Remote Sens. 58 (10) (1992) 1417–1423.

[36] R. Pande-Chhetri, A. Abd-Elrahman, De-striping hyperspectral imagery using wavelet transform and adaptive frequency domain filtering, ISPRS J. Photogramm. Remote Sens. 66 (5) (2011) 620–636.

[37] P. Rakwatin, W. Takeuchi, Y. Yasuoka, Stripe noise reduction in modis data by combining histogram matching with facet filter, IEEE Trans. Geosci. Remote Sens. 45 (6) (2007) 1844–1856.

[38] H. Shen, L. Zhang, A map-based algorithm for destriping and inpainting of remotely sensed images, IEEE Trans. Geosci. Remote Sens. 47 (5) (2009) 1492–1502.

[39] R. Srinivasan, M. Cannon, J. White, Landsat data destriping using power spectral filtering, Opt. Eng. 27 (11) (1988) 939–943.

[40] D.W.J. Stein, S.G. Beaven, L.E. Hoff, E.M. Winter, Anomaly detection from hyperspectral imagery, IEEE Signal Process. Mag. 19 (1) (2002) 58–69.

[41] L. Sun, R. Neville, K. Staenz, H.P. White, Automatic destriping of Hyperion imagery based on spectral moment matching, Can. J. Remote Sens. 34 (sup1) (2008) S68–S81.

[42] Y.J. Sun, T.Z. Huang, T.H. Ma, Y. Chen, in: Remote sensing image stripe detecting and destriping using the joint sparsity constraint with iterative support detection, 2019, doi:10.3390/rs11060608.

[43] J. Torres, S.O. Infante, Wavelet analysis for the elimination of striping noise in satellite images, Opt. Eng. 40 (7) (2001) 1309–1314.

[44] F. Tsai, W.W. Chen, Striping noise detection and correction of remote sensing images, IEEE Trans. Geosci. Remote Sens. 46 (12) (2008) 4122–4131.

[45] M. Wang, X. Zheng, J. Pan, B. Wang, Unidirectional total variation destriping using difference curvature in modis emissive bands, Infrared Phys. Technol. 75 (2016) 1–11.

[46] Y.T. Wang, X.L. Zhao, T.X. Jiang, L.J. Deng, T.H. Ma, Y.T. Zhang, T.Z. Huang, A total variation and group sparsity based tensor optimization model for video rain streak removal, Signal Process. Image Commun. doi:10.1016/j.image.2018.11.0080923-5965.

[47] Z. Wang, A.C. Bovik, H.R. Sheikh, E.P. Simoncelli, Image quality assessment: from error visibility to structural similarity, IEEE Trans. Image Process. 13 (4) (2004) 600–612.

[48] M. Wegener, Destriping multiple sensor imagery by improved histogram matching, Int. J. Remote Sens. 11 (5) (1990) 859–875.

[49] M.P. Weinreb, R. Xie, J.H. Lienesch, D.S. Crosby, Destriping goes images by matching empirical distribution functions, Remote Sens. Environ. 29 (2) (1989) 185–195.

[50] J.H. Yang, X.L. Zhao, J.J. Mei, S. Wang, T.H. Ma, T.Z. Huang, Total variation and high-order total variation adaptive model for restoring blurred images with cauchy noise, Comput. Math. Appl. 77 (5) (2019) 1255–1272.

[51] W. Yin, W. Deng, Y. Zhang, Group sparse optimization by alternating direction method, SPIE Opt. Eng. Appl. (2013) 88580R–88580R–15.

[52] Y. Zhang, G. Zhou, L. Yan, T. Zhang, A destriping algorithm based on tv-stokes and unidirectional total variation model, Optik Int. J. Light Electron. Opt. 127 (1) (2016) 428–439.

[53] X.L. Zhao, F. Wang, M.K. Ng, A new convex optimization model for multiplicative noise and blur removal, SAME J. Imaging Sci. 7 (1) (2014) 456–475.

[54] X.L. Zhao, W. Wang, T.Y. Zeng, T.Z. Huang, M.K. Ng, Total variation structured total least squares method for image restoration, SIAM J. Sci. Comput. 35 (6) (2013) B1304–B1320.

[55] Y.B. Zheng, T.Z. Huang, T.Y. Ji, X.L. Zhao, T.X. Jiang, T.H. Ma, Low-rank tensor completion via smooth matrix factorization, Appl. Math. Model. 70 (2019) 677–695.

[56] G. Zhou, H. Fang, C. Lu, S. Wang, Z. Zuo, J. Hu, Robust destriping of modis and hyperspectral data using a hybrid unidirectional total variation model, Optik Int. J. Light Electron. Opt. 126 (7) (2015) 838–845.

[57] Z. Zhu, G. Cai, Y.W. Wen, Adaptive box-constrained total variation image restoration using iterative regularization parameter adjustment method, Int. J. Pattern Recognit. Artif. Intell. 29 (7) (2015) 1554003.